

Clusters of galaxies up to $z = 1.5$ identified from photometric data of the Dark Energy Survey and unWISE

Z. L. Wen^{1,2*} and J. L. Han^{1,2,3}

1. National Astronomical Observatories, Chinese Academy of Sciences, 20A Datun Road, Chaoyang District, Beijing 100012, China

2. CAS Key Laboratory of FAST, NAOC, Chinese Academy of Sciences, Beijing 100101, China

3. School of Astronomy, University of Chinese Academy of Sciences, Beijing 100049, China

Accepted XXX. Received YYY; in original form ZZZ

ABSTRACT

Using photometric data from the Dark Energy Survey and the Wide-field Infrared Survey Explorer, we estimate photometric redshifts for 105 million galaxies using the nearest-neighbour algorithm. From such a large data base, 151 244 clusters of galaxies are identified in the redshift range of $0.1 < z \lesssim 1.5$ based on the overdensity of the total stellar mass of galaxies within a given photometric redshift slice, among which 76 826 clusters are newly identified and 30 477 clusters have a redshift $z > 1$. We cross-match these clusters with those in the catalogues identified from the X-ray surveys and the Sunyaev–Zel’dovich (SZ) effect by the *Planck*, South Pole Telescope and Atacama Cosmology Telescope surveys, and get the redshifts for 45 X-ray clusters and 56 SZ clusters. More than 95 percent SZ clusters in the sky region have counterparts in our catalogue. We find multiple optical clusters in the line of sight towards about 15 percent of SZ clusters.

Key words: catalogues — galaxies: clusters: general — galaxies: distances and redshifts.

1 INTRODUCTION

As the largest virialized systems in the Universe, clusters of galaxies trace density peaks in the the large-scale structure. Galaxy clusters have been identified from the survey data in optical, X-ray and millimeter bands (e.g. Abell et al. 1989; Piffaretti et al. 2011; Wen et al. 2012; Böhringer et al. 2013; Planck Collaboration et al. 2016; ?; Hilton et al. 2021). Based on multiband optical photometric observations, clusters of galaxies can be found through the red sequence of galaxies (e.g. Oguri 2014; Rykoff et al. 2014) or photometric redshifts of galaxies (e.g. Wen et al. 2012; Yang et al. 2021; Zou et al. 2021). The X-ray observation data show the X-ray emission from hot intracluster medium. The Sunyaev–Zel’dovich (SZ) effect at the millimeter wavelengths has the advantage to detect massive clusters up to high redshifts (Carlstrom et al. 2002).

The latest data sets observed for the southern Galactic cap provide an excellent opportunity to uncover clusters at high redshifts. The Dark Energy Survey (DES; Dark Energy Survey Collaboration et al. 2016) released photometric data at five bands for a sky area of 5000 deg² region down to a limit of $i \sim 24$ magnitude, which is deep enough to detect clusters up to $z \sim 1.5$. A large number of clusters of galaxies have been identified from the DES data (Rykoff et al. 2016; Aguena et al. 2021; Yang et al. 2021; Zou et al. 2021), but mostly of $z < 1$. In the DES sky region, millimeter survey data have been obtained by the South Pole Telescope (SPT; Carlstrom et al. 2011)

and the Atacama Cosmology Telescope (ACT; Swetz et al. 2011). About 850 and 1800 clusters have been already identified by using the SZ effect from the SPT and ACT survey data, respectively (Bleem et al. 2015, 2020; Huang et al. 2020; Hilton et al. 2021).

In this paper, we combine the DES optical data with the mid-infrared data from the Wide-field Infrared Survey Explorer (WISE; Wright et al. 2010) to identify clusters of galaxies. In Section 2, we cross-match the DES data with the WISE data for common galaxies, and estimate their photometric redshifts and stellar masses. In Section 3, we identify clusters of galaxies from the estimated photometric redshift data. In Section 4, we compare the identified clusters with those previously known in the sky region. A summary is presented in Section 5.

Throughout this paper, we assume a flat Lambda cold dark matter cosmology taking $H_0 = 70 \text{ km s}^{-1} \text{ Mpc}^{-1}$, $\Omega_m = 0.3$, and $\Omega_\Lambda = 0.7$.

2 PHOTOMETRIC REDSHIFTS AND STELLAR MASSES

Identification of galaxy clusters requires a large number of galaxies with known redshifts. The photometric redshifts can be used for the purpose, and can be estimated from photometric data (Wen & Han 2021). In addition, stellar masses of galaxies can be derived based on the mid-infrared luminosity of galaxies, which is useful to identify density peaks.

* E-mail: zhonglue@nao.cas.cn

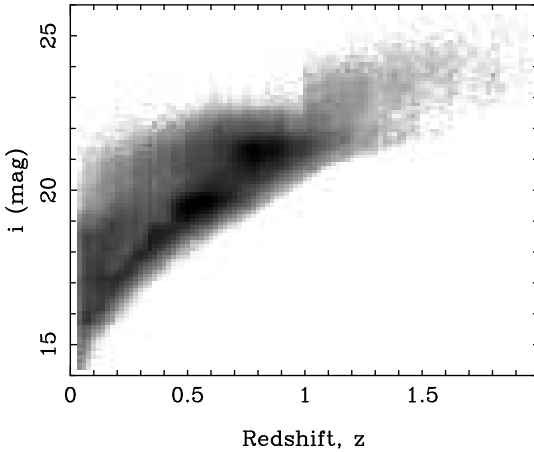


Figure 1. The training sample has a wide distribution in the redshift and is deep enough in the i -band.

2.1 Photometric data of galaxies

The DES¹ made photometric observations at five broad optical bands (*grizy*), covering the southern Galactic cap of ~ 5000 deg² (Dark Energy Survey Collaboration et al. 2016). The survey reaches a 10σ depth of $i \sim 24$ (AB magnitude) for point sources. The median full width at half-maximum of the point spread function is 0.88 arcsec in the i -band. From the latest public DES data release 2 (DR2, Abbott et al. 2021), we get 399 million galaxies detected above 5σ in at least one band and with the magnitudes at least in the r , i and z bands. The galaxies are selected with the flags of $\text{IMAFLAGS}_{\text{ISO}} = 0$, $\text{FLAGS} < 4$ and an extended morphology classification of $\text{SPREAD_MODEL} \geq 2$.

The WISE observed the whole sky at four mid-infrared bands of W1, W2, W3, and W4 (Wright et al. 2010). The angular resolutions of the WISE are 6.1 and 6.5 arcsec in the W1 and W2 bands, respectively. We use the W1 and W2-band data from the five-year coadd image data², named as unWISE, which is deep enough to detect massive galaxies up to a redshift of $z \sim 2$ (Lang 2014; Schlafly et al. 2019). The unWISE catalogue contains 208 million sources with W1-band data available in the sky coverage of the DES DR2.

The spread function of the unWISE data is much wider than that of the DES data, so that very close DES galaxies may not be resolved in the unWISE. As in Wen & Han (2021), we perform one-to-one match between the DES galaxies and the unWISE sources within a radius of 2 arcsec. The closest source within this radius is adopted for the targeted object. The such matched 105 million objects are named as DES \times unWISE galaxies in this paper.

2.2 Photometric redshifts of galaxies

Photometric redshifts of DES \times unWISE galaxies are determined based on the galaxy colours and their nearest-neighbour spectroscopic redshifts in a training sample, following Wen & Han (2021).

The training sample of spectroscopic redshifts are obtained from the Sloan Digital Sky Survey (SDSS) data release 16 (Ahumada et al. 2020), PRIMUS DR1 (Cool et al. 2013), VIPERS PDR2 (Scodggio et al. 2018), VVDS (Le Fèvre et al. 2013),

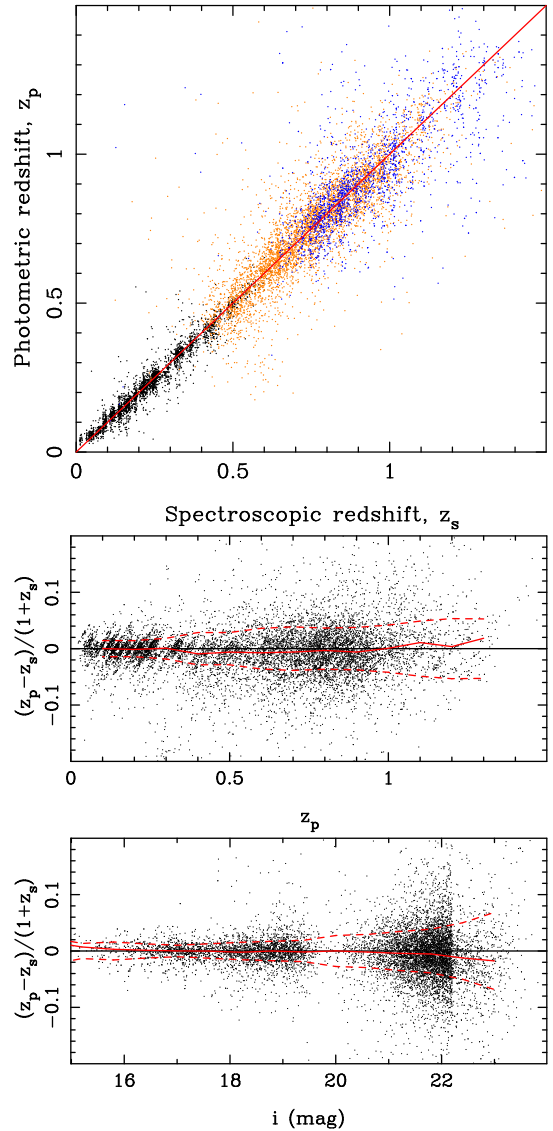


Figure 2. Upper panel: verification of estimated redshifts by comparing them with spectroscopic redshifts of galaxies in the GAMA (black), VIPERS DR2 (qFlag=2–3, orange) and DEEP2 (blue) data. A great consistence is shown in a very wide range of redshift, though the dispersion of data becomes larger at higher redshifts. Middle panel: the difference between estimated photometric redshifts and spectroscopic redshifts plotted against photometric redshift. Bottom panel: the difference plotted against i -band magnitude. The dashed lines indicate $\pm\sigma_{\Delta z}$ and the solid line indicates the bias.

and 3D-HST (Momcheva et al. 2016). We adopt the same redshift flags as in Wen & Han (2021), and get spectroscopic redshifts for 460 653 galaxies, among which 335 896 galaxies have DES \times unWISE magnitudes in at least six bands of *grizyW1*. To have a good redshift coverage for faint galaxies, we also include 6341 galaxies from the Hyper Suprime-Cam Subaru Strategic Program (HSC-SSP) \times unWISE data (Wen & Han 2021) into the training sample, which have spectroscopic redshifts in the range of $1 < z < 2$. For these galaxies, the HSC-SSP *grizy* magnitudes are converted to the DES *grizy* magnitudes following conversion equations in Abbott et al. (2021). In total, we have 342 237 galaxies from the DES \times unWISE and HSC-SSP \times unWISE for the training sample. Fig. 1 shows the wide distribution of galaxies in the

¹ <https://www.darkenergysurvey.org/>

² <http://unwise.me/>

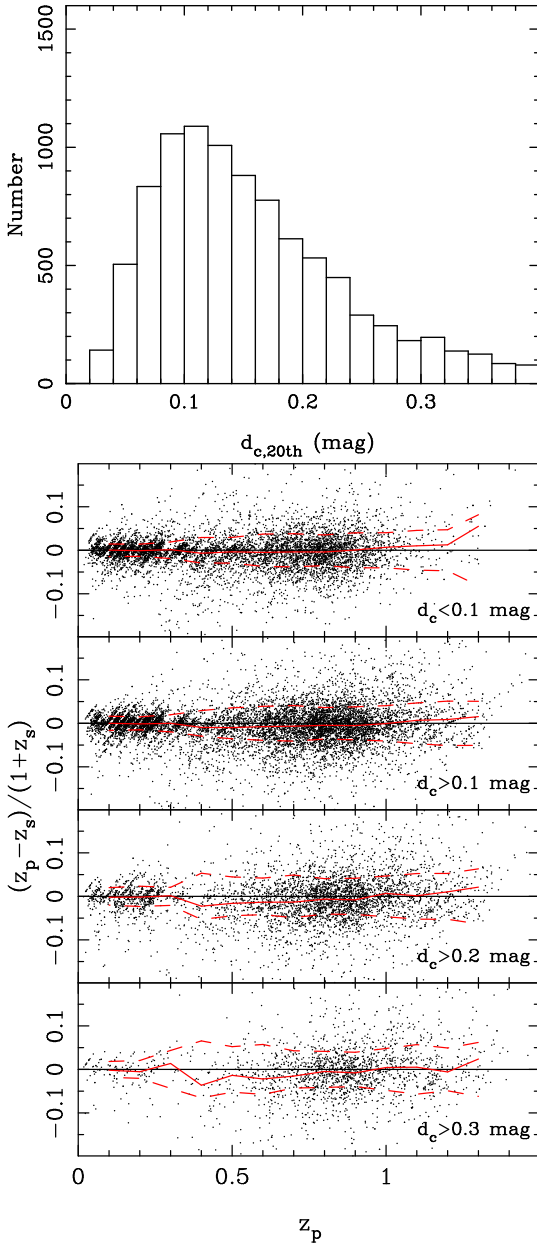


Figure 3. Upper: distribution of total colour offset of the 20th neighbour in the multidimensional colour space. Lower: redshift differences for four redshift estimates by using only the galaxies among the 20 nearest neighbours with colour offsets of $d_c < 0.1$ mag, or $d_c > 0.1$ mag, or $d_c > 0.2$ mag or $d_c > 0.3$ mag, respectively. The dashed lines indicate $\pm\sigma_{\Delta z}$ and the solid line indicates the bias.

redshift-magnitude diagram. The faint end of the training sample extends to $i > 24$ and the redshift extends to $z > 1.5$, suggesting that the training sample can be used to faint galaxies near the limit of the DES×unWISE galaxies.

For each of the DES×unWISE galaxies, we estimate the photometric redshift as being the median of the spectroscopic redshifts of 20 nearest neighbours in multidimensional colour space ($g-r$, $r-i$, $i-z$, $i-y$, $i-W1$, and $W1-W2$) of the training sample (De Vicente et al. 2016; Wen & Han 2021). The uncertainty of each photometric redshift σ_{z_p} is estimated as being the standard deviation of the spectroscopic redshifts of these 20 nearest neighbours. If an object has many neighbours from the training objects in the

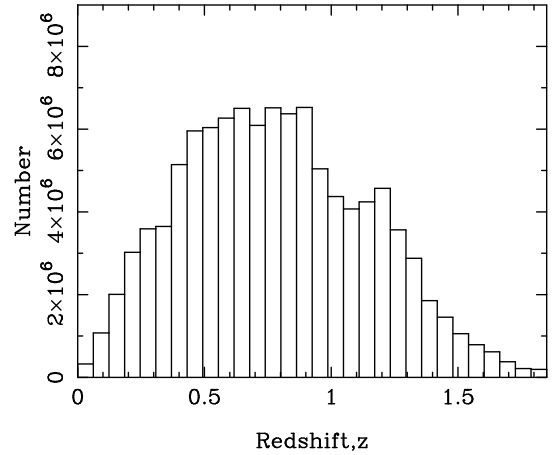


Figure 4. Number distribution of photometric redshifts of DES×unWISE galaxies.

colour space with a similar redshift, the photometric redshift would have a small uncertainty; if a galaxy is located in a sparse region in the colour space where less objects are available, the photometric redshift would have to be estimated from the largely scattered spectroscopic redshifts and thus has a large uncertainty. Therefore the uncertainty of each photometric redshift indicates the reliability of the estimated photometric redshift.

We verify the accuracy of such estimated redshifts by comparing them with spectroscopic redshifts of galaxies by using an independent testing sample from the GAMA DR2 (Liske et al. 2015), VIPERS PDR2 (Scodeggio et al. 2018), and DEEP2 DR4 (Matthews et al. 2013). Most galaxies in the GAMA data have a low redshift of $z < 0.5$. The VIPERS PDR2 data have a high (> 99 percent) confidence on redshift for the galaxies with $qFlag=3-4$ and have been included in the training sample. Here, we adopt the VIPERS redshifts for the galaxies at $0.5 < z < 1.2$ with $qFlag=2-3$, which have a slightly lower but also excellent (> 95 percent) confidence. The DEEP2 galaxies mostly have redshifts in the range of $0.7 < z < 1.4$. These data are magnitude-limited without any colour selection. We discard the common galaxies with those in the training sample and obtain a testing sample of 9857 galaxies at $z \lesssim 1.4$. Their photometric redshifts are estimated and compared with the spectroscopic redshifts, as shown in Fig. 2. The redshift difference, $(z_p - z_s)/(1 + z_s)$, is plotted against the photometric redshift (middle panel). The systematic bias, defined as the median value of the difference, is generally small at $z < 1$ and the largest bias is about -0.008 at $z \sim 0.5$. The bias is about 0.01 at $z > 1.1$. The redshift uncertainty, defined as $\sigma_{\Delta z} = 1.48 \times \text{median}(|z_p - z_s|/(1 + z_s))$, generally increases with redshift from 0.013 at $z \sim 0.1$ to 0.052 at $z \sim 1.3$. The redshift difference also slightly depends on i -band magnitude (bottom panel of Fig. 2). Naturally the galaxies at the faint end have the largest bias, which is about -0.018 at $i = 23$.

In our algorithm for photometric redshifts of galaxies, we fix the number of 20 nearest neighbours to estimate photometric redshifts. Some of the neighbours may have a large colour offset from the targeted galaxy in the colour space, especially at high redshifts with sparse training samples. We test if such neighbours with large offsets cause a significant bias for the estimated photometric redshift. In the upper panel of Fig. 3, we show the total colour offset distribution of the 20th nearest neighbour in the multidimensional colour space of $g-r$, $r-i$, $i-z$, $i-y$, $i-W1$, and $W1-W2$

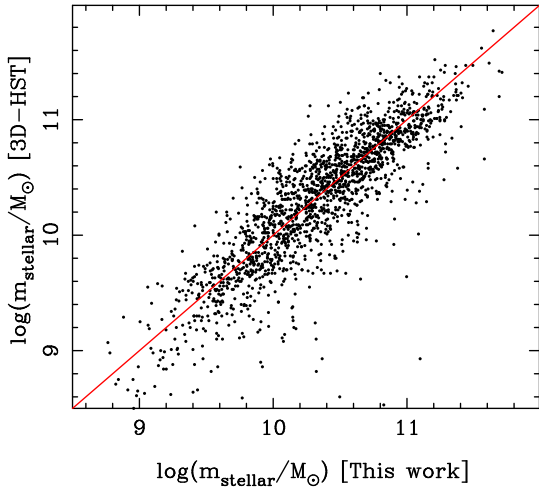


Figure 5. Comparison of our stellar masses estimated from W1-band luminosity with the accurate values obtained from the 3D-HST survey shows a good agreement. The solid line indicates the equality.

for the 9857 testing galaxies. The distribution has a median value of 0.14 mag, and 12 per cent of galaxies have offsets larger than 0.3 mag. In the lower panels of Fig. 3, we calculate four testing photometric redshifts by using the training galaxies among the 20 nearest neighbours with colour offsets $d_c < 0.1$ mag, or only galaxies with $d_c > 0.1$ mag, or > 0.2 mag or > 0.3 mag, respectively. We compare the redshift differences and find that the biases are not significant except for the cases with small number of galaxies.

Using the training sample of 342 237 galaxies, we then estimate the photometric redshifts for 105 million DES×unWISE galaxies. The obtained photometric redshifts have a wide distribution up to $z \sim 1.7$ with a peak at $z \sim 0.7$ (see Fig. 4), which enable us to identify a large sample of clusters to redshifts $z > 1$.

2.3 Stellar mass of galaxies

With photometric redshifts estimated, the stellar masses, m_{stellar} , can be derived for the 105 million galaxies in the DES×unWISE catalogue from the W1-band luminosity following the procedures of our previous work (Wen & Han 2021). Comparison of our estimates with the accurate values obtained from the 3D-HST survey (Momcheva et al. 2016), as shown in Fig. 5, shows that they are in good agreement, with a scatter of only 0.23 dex.

3 CLUSTERS IDENTIFIED FROM THE DES×UNWISE GALAXIES

Following Wen & Han (2021), we identify a cluster of galaxies based on the overdensity of galaxy stellar mass within a photometric redshift slice around each massive galaxy of $m_{\text{stellar}} \geq 5 \times 10^{10} M_{\odot}$ that is temporally assumed to be the brightest cluster galaxy (BCG) of a cluster candidate. The redshift of a cluster candidate, z (or z_{cl} for a finally identified cluster), is taken to be the median value of the photometric redshifts of member galaxy candidates within a photometric redshift slice of $z \pm \Delta z$ and a projected radius of r_1 . The half of the slice thickness is taken as being

$$\Delta z = \begin{cases} 0.04(1+z) & \text{for } z \leq 0.7 \\ 0.15z - 0.037 & \text{for } z > 0.7 \end{cases}, \quad (1)$$

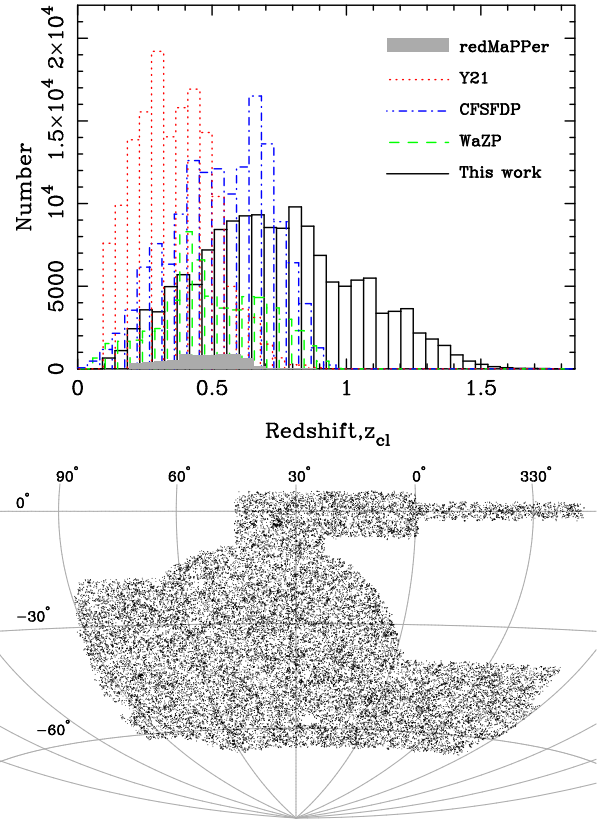


Figure 6. Upper panel: The redshift distribution of 151 244 clusters in our catalogue compared with those in the DES footprint, including clusters from the catalogues of redMaPPer (Rykoff et al. 2016), Y21 (only clusters with more than 10 members in Yang et al. 2021), CFSFDP (Zou et al. 2021), WaZP (Aguena et al. 2021). Lower panel: The sky distribution of newly identified high redshift clusters of $z_{\text{cl}} > 1.0$.

and the projected radius is taken as

$$r_1 = 1.0 E(z)^{-2/3} \text{ Mpc}, \quad (2)$$

where $E(z) = \sqrt{\Omega_{\Lambda} + \Omega_m(1+z)^3}$ (there is a minor mistake for the equation of r_1 in Wen & Han 2021). Member galaxy candidates are excluded if their photometric redshifts are unreliable with $\sigma_{\text{zp}} > 2\Delta z$. From these member galaxy candidates, we get the total stellar mass, m_{stellar,r_1} within the radius r_1 . The cluster radius, r_{500} , within which the mean density of a cluster is 500 times of the critical density of the universe, is estimated from a calibrated $r_{500}-m_{\text{stellar},r_1}$ relation based on a sample of X-ray clusters (Wen & Han 2021). Then, the total stellar mass within the estimated radius r_{500} is calculated from the galaxy data, which is later defined as the richness of a cluster, λ_{500} , as in Wen & Han (2021). The overdensity is expressed as the detection signal-to-noise ratio, SNR, which is calculated based on the overdensity of galaxy stellar mass within a projected radius of 0.5 Mpc related to the density fluctuations in the surrounding regions of the same redshift slice. A cluster is identified with the threshold of $\text{SNR} \geq 5$ and a richness of $\lambda_{500} \geq 15$, and also the number of member galaxy candidates within r_{500} as being $N_{\text{gal}} \geq 6$. Finally, the repeated entries within a photometric redshift slice of $z \pm 1.5\Delta z$ and a projected distance of $1.5 r_{500}$ are cleaned so that only one cluster candidate with the largest richness is adopted. The low-redshift clusters of $z_{\text{cl}} < 0.1$ are discarded because some bright BCGs have the flag

Table 1. The 151 244 clusters of galaxies identified from the DES×unWISE data.

Cluster ID (1)	Name (2)	R.A. (3)	Dec. (4)	z_{cl} (5)	i_{BCG} (6)	$W1_{BCG}$ (7)	SNR (8)	r_{500} (9)	λ_{500} (10)	M_{500} (11)	N_{gal} (12)	Other catalogues (13)
1	WH J000000.5+021911	0.00200	2.31979	0.4192	18.738	17.964	6.75	0.549	18.77	0.86	15	WH21
2	WH J000001.3−640959	0.00555	−64.16639	0.6423	18.565	17.360	10.17	0.673	36.48	1.62	12	
3	WH J000001.4−521956	0.00563	−52.33236	0.5829	19.249	18.207	6.00	0.590	21.61	0.98	12	redMaPPer
4	WH J000002.3−475113	0.00943	−47.85358	0.7734	20.239	18.481	5.48	0.487	17.47	0.80	13	CFSFDP
5	WH J000002.8−474415	0.01186	−47.73740	0.3169	17.305	17.307	7.53	0.548	17.18	0.79	11	
6	WH J000003.1−033245	0.01274	−3.54574	0.6056	18.754	17.483	14.00	0.722	43.60	1.92	22	WHL
7	WH J000003.8−010154	0.01592	−1.03153	0.7327	19.759	18.242	6.06	0.621	26.65	1.20	10	WaZP
8	WH J000003.9−525115	0.01610	−52.85407	0.7657	20.561	18.513	6.34	0.559	20.93	0.95	12	
9	WH J000004.2−393257	0.01733	−39.54926	0.6064	19.742	18.163	6.69	0.542	20.50	0.93	13	CFSFDP
10	WH J000004.2+021941	0.01742	2.32799	0.6228	19.247	17.721	6.47	0.541	20.33	0.92	9	WHL

Note. Column 1: Cluster ID; Column 2: Cluster name with J2000 coordinates of cluster; Columns 3 and 4: Right Ascension (R.A. J2000) and Declination (Dec. J2000) of cluster BCG (in degree); Column 5: cluster redshift z_{cl} ; Columns 6–7: BCG magnitudes (AB system) in i and $W1$ bands, respectively; Column 8: SNR for cluster detection; Column 9: cluster radius, r_{500} , in Mpc; Column 10: cluster richness; Column 11: derived cluster mass, in units of $10^{14} M_{\odot}$; Column 12: number of member galaxy candidates within r_{500} ; Column 13: Reference notes for previously known clusters: WHL (Wen et al. 2012; Wen & Han 2015), SPT (Bleem et al. 2015, 2020; Huang et al. 2020), redMaPPer (Rykoff et al. 2016), WHY18 (Wen et al. 2018), RASS (Klein et al. 2019), ACT (Hilton et al. 2021), WH21 (Wen & Han 2021), Y21 (Yang et al. 2021), CFSFDP (Zou et al. 2021), WaZP (Aguena et al. 2021).

(This table is available in its entirety in a machine-readable form.)

of IMAFLAGS_ISO≠0 and are not included in the DES×unWISE data.

From the DES×unWISE galaxies with estimated redshifts, we find 151 244 clusters as listed in Table 1, among which 76 826 clusters are newly identified and 74 418 clusters are previously known (Bleem et al. 2015, 2020; Wen & Han 2015, 2021; Rykoff et al. 2016; Wen et al. 2018; Klein et al. 2019; Huang et al. 2020; Aguena et al. 2021; Hilton et al. 2021; Yang et al. 2021; Zou et al. 2021). Cluster masses are derived by using the mass–richness relation in Wen & Han (2021). The 2 454 302 member galaxy candidates within r_{500} for these clusters are also publicly available on web-page³. Fig. 6 shows the redshift distribution of identified clusters in the range of $0.1 < z_{cl} \lesssim 1.5$ with a wide peak at about $z_{cl} \sim 0.7$. Much more clusters are found at higher redshifts than previous cluster findings. We get 30 477 clusters with a redshift of $z_{cl} > 1$, and they are widely distributed in the sky (see low panel of Fig. 6).

To evaluate the accuracy of cluster photometric redshift, in Fig. 7, we compare the estimated cluster redshifts with available spectroscopic redshifts for their BCGs of 8739 clusters plus the spectroscopic redshifts for 32 clusters of $z > 0.9$ from the NASA/IPAC Extragalactic Database (NED)⁴. The uncertainty of cluster redshift, defined as $1.48 \times \text{median}(|z_{cl} - z_{BCG,s}|/(1 + z_{BCG,s}))$, is about 0.013. Only 1.6 per cent of our clusters have photometric redshifts that deviate from spectroscopic redshifts larger than $0.05(1 + z)$. A few outliers may be a false identification in the case that foreground or background galaxies are miss taken as BCGs. As shown in Fig. 2, the uncertainty of galaxy photometric redshift rapidly increases at $z > 0.9$, making that the estimated cluster redshift has a larger uncertainty and a systematic bias of about 0.02 at $z_{cl} \sim 1$. Due to the small number of clusters with spectroscopic redshift measurements, the uncertainty of cluster redshifts is hard to assess at $z > 1$.

We visually inspect the colour images of the identified clus-

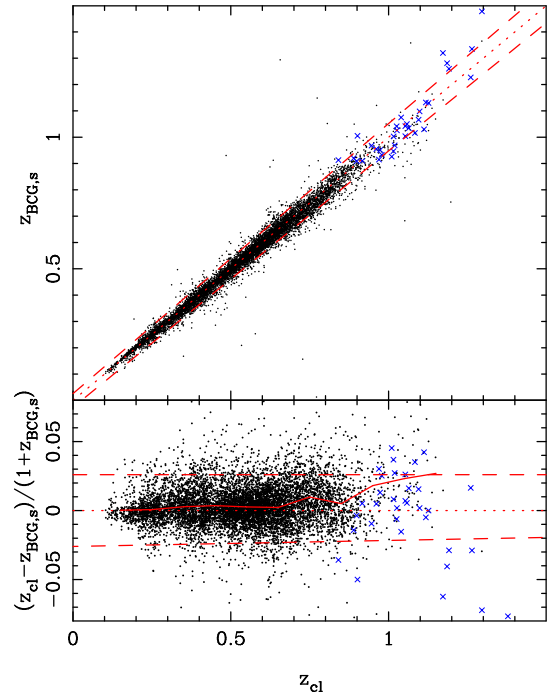


Figure 7. Comparison between the spectroscopic redshifts of BCGs with cluster photometric redshifts. The dashed lines indicate the 2σ uncertainty. Blue crosses are clusters with known spectroscopic redshifts we obtained from the NED.

ters from the DES×unWISE data for a verification of our catalogue, especially at high redshifts. Fig. 8 shows the DES colour (r_{iz}) images for three rich clusters at redshifts of $z_{cl} = 1.0055$, 1.0959, and 1.2602, respectively. The clusters have a richness of $\lambda_{500} = 106.19$, 126.85, and 139.60, respectively, and show many red galaxies concentrated. To check the clusters at higher redshifts, we inspect the colour images of both DES and HSC-SSP Deep data for the clusters in a small overlapped region. Fig. 9

³ http://zmtt.bao.ac.cn/galaxy_clusters/

⁴ <http://ned.ipac.caltech.edu/>

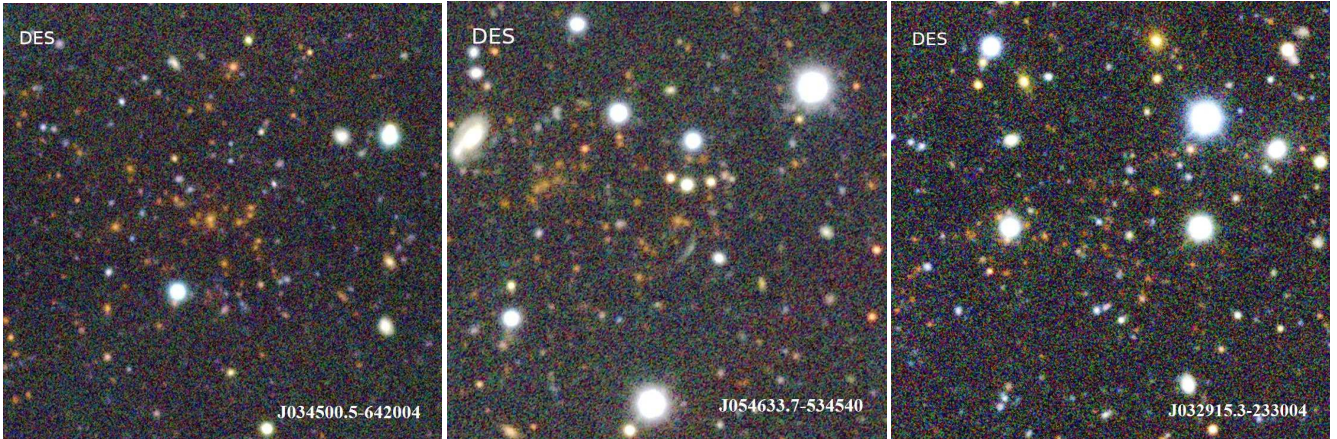


Figure 8. DES composite (*riz*) colour images of three identified clusters at redshifts of $z_{cl} = 1.0055$ (left), 1.0959 (middle), and 1.2602 (right) and with richnesses of $\lambda_{500} = 106.19$, 126.85, and 139.60, respectively. The images have a size of 2 arcmin \times 2 arcmin.

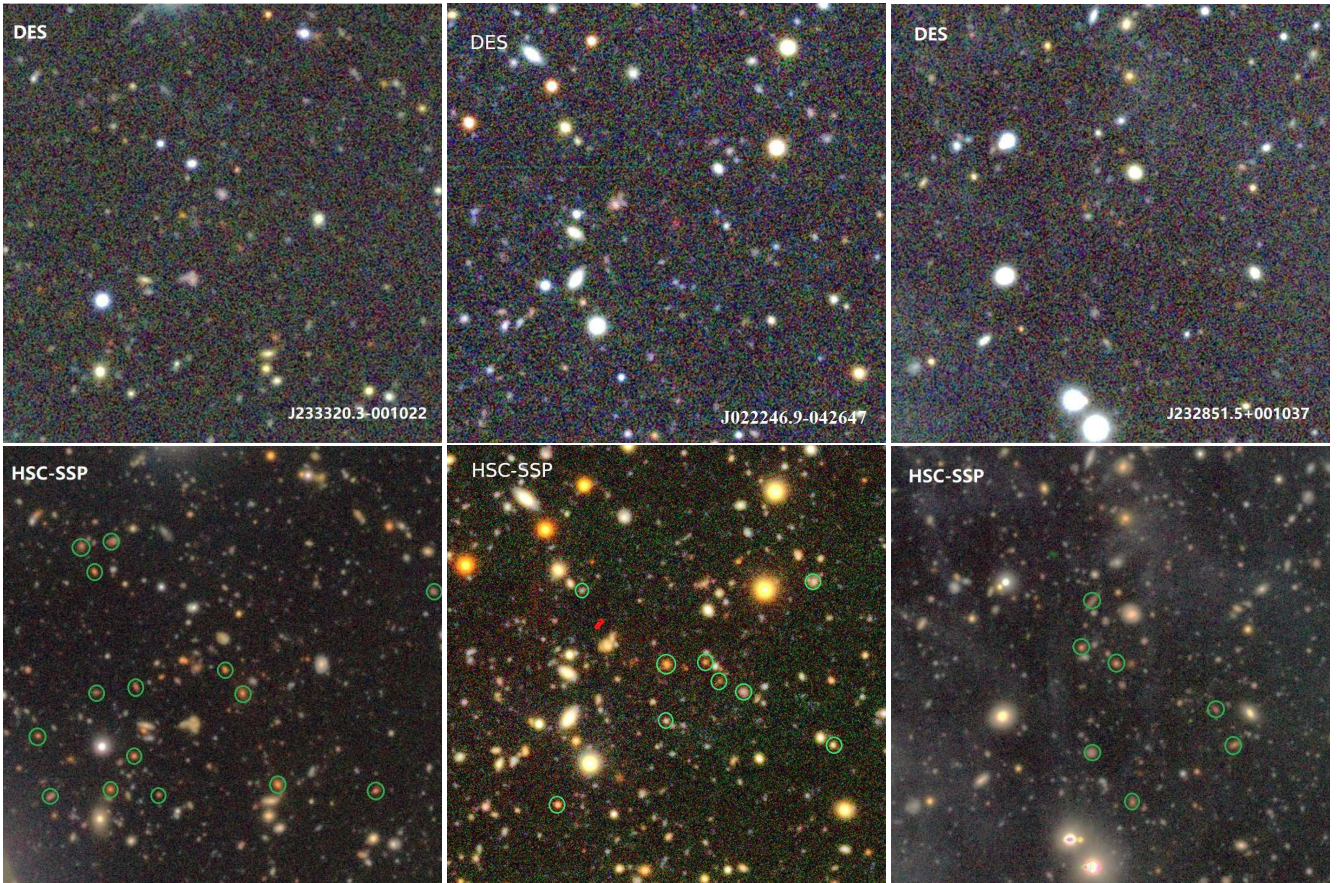


Figure 9. Upper panels: DES colour images for three clusters at higher redshifts of $z_{cl} = 1.3046$ (left), 1.3510 (middle), and 1.3957 (right) with richnesses of $\lambda_{500} = 42.03$, 27.26, and 20.77, respectively. Lower panels: same clusters as in the upper panels but the HSC-SSP Deep colour images. The green circles indicate the member galaxy candidates of the clusters.

also shows the colour images for three high-redshift clusters at $z_{cl} = 1.3046$, 1.3510, and 1.3957, respectively, and with a richness of $\lambda_{500} = 42.03$, 27.26, and 20.77, respectively. Only a few massive galaxies are selected as member galaxy candidates. They are very indistinct in the DES images, but clearly shown in the HSC-SSP Deep images.

4 COMPARISON OF CLUSTER PROPERTIES IN DIFFERENT CATALOGUES

Cluster finding algorithms have been applied to the DES data and result in many catalogues of galaxy clusters, including the red-sequence matched-filter Probabilistic Percolation cluster finder (redMaPPer; Rykoff et al. 2014), an extended halo-based group finder (Y21; Yang et al. 2021), clustering by Fast Search and Find

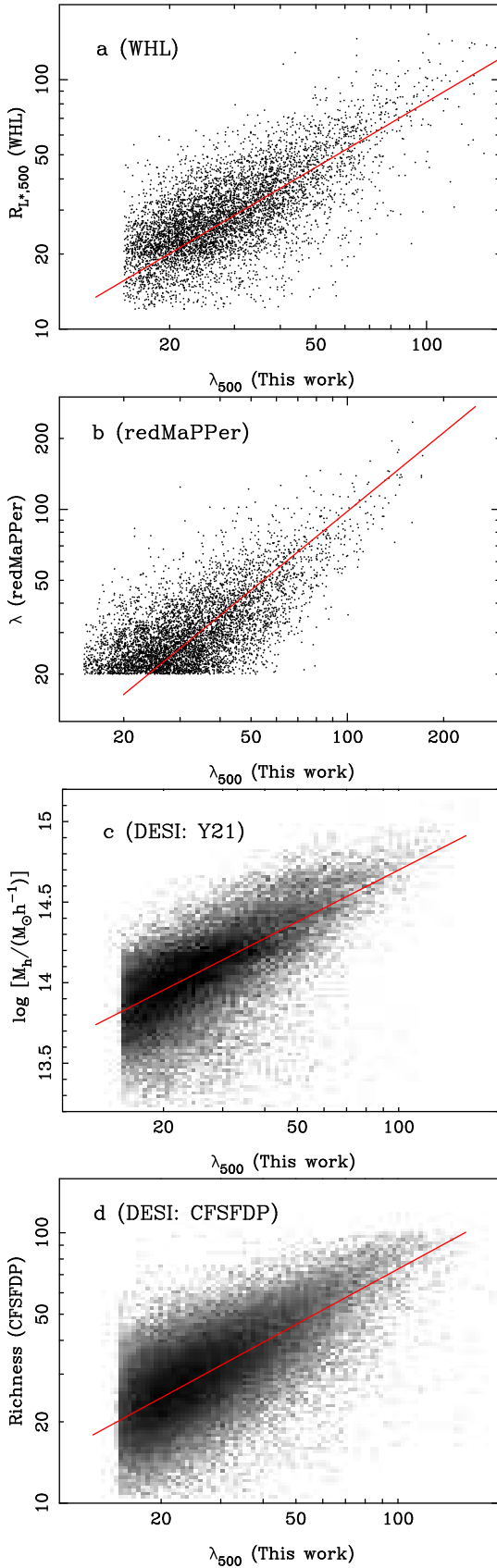


Figure 10. Comparison of our cluster richness with the richness (or halo mass) of WHL (panel a), redMaPPer (panel b), and DESI (panels c and d). The red lines are the best fits of the correlation.

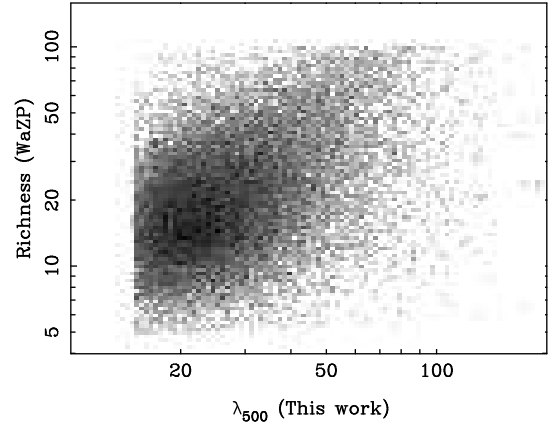


Figure 11. Correlation of our cluster richness with the WaZP richness.

of Density Peaks (CFSFDP; Zou et al. 2021) and the Wavelet Z Photometric (WaZP; Aguena et al. 2021). In the DES footprint, a large sample of X-ray clusters have been identified from the combined data of *ROSAT* and the DES (Klein et al. 2019). Thousands of massive SZ clusters have been identified up to a high redshift of $z > 1$ from the *Planck*, SPT, and ACT surveys (Planck Collaboration et al. 2016; Bleem et al. 2020; Hilton et al. 2021). Here, we compare the properties of clusters in our catalogue from the DES with those in previous catalogues.

4.1 Comparison with optical clusters

4.1.1 WHL clusters

Previously, we identified a sample of 158 103 clusters from the SDSS data using the similar algorithm (Wen et al. 2012; Wen & Han 2015, WHL hereafter). The richness is defined to be the total luminosity of member galaxies within an estimated r_{500} .

There are 11685 WHL clusters of $z \geq 0.1$ in the DES footprint, of which 6360 (54 per cent) clusters have counterparts in this work within a redshift difference of $0.05(1+z)$ and a projected distance of $1.5 r_{500}$. We find that the richnesses are well correlated in the two catalogues (see Fig. 10 a)

$$\log R_{L^*,500} = (0.87 \pm 0.01) \log \lambda_{500} + (0.17 \pm 0.02). \quad (3)$$

4.1.2 redMaPPer clusters

The redMaPPer algorithm identifies clusters in multiband surveys based on the red-sequence feature of cluster galaxies (Rykoff et al. 2014). The algorithm first calibrates a red sequence model of clusters as a function of redshift by using a training sample. Then, the red sequence model is applied to photometric data to search clusters. For each identified cluster, the algorithm estimates a membership probability of red galaxies brighter than $0.2 L^*$ following an iteratively matched-filter technique. The cluster richness is defined to be the sum over the members with various probabilities. There are 6729 redMaPPer clusters at $0.2 < z \lesssim 0.8$ in the DES Y1 data covering a sky area of $\sim 1800 \text{ deg}^2$ (Rykoff et al. 2016).

Cross-matching shows that 5792 (~ 86 per cent) redMaPPer clusters are found in Table 1 within a redshift difference of $0.05(1+z)$ and a projected distance of $1.5 r_{500}$. The redMaPPer richness has a good correlation with our richness (Fig. 10 b), with the best

fit by a power law

$$\log \lambda_{500} = (0.90 \pm 0.01) \log \lambda(\text{redMaPPer}) + (0.21 \pm 0.02). \quad (4)$$

4.1.3 DESI clusters

Dark Energy Spectroscopic Instrument (DESI) legacy imaging surveys are composed of three optical surveys, i.e. the Beijing-Arizona Sky Survey (Zou et al. 2017), the DES and the Mayall survey (Zhou et al. 2018). Recently, two large catalogues of clusters/groups have been obtained from the data of DESI legacy imaging surveys (Yang et al. 2021; Zou et al. 2021).

Using photometric or spectroscopic redshifts of galaxies, Yang et al. (2021) applied an extend halo-based group finder to the DESI legacy imaging surveys and identified 6.4 million groups with at least three members. The halo masses of the groups are estimated based on the total luminosities of group member galaxies. In the DES footprint, 152 035 clusters of $z > 0.1$ have at least 10 members. Our richness has a tight correlation with their halo mass by a power law (Fig. 10 c),

$$\log M_h = (1.08 \pm 0.01) \log \lambda_{500} - (1.45 \pm 0.02), \quad (5)$$

where M_h is in units of $10^{14} M_\odot h^{-1}$.

Zou et al. (2021) applied a similar algorithm to ours to have identified galaxy clusters using photometric redshifts of galaxies in the DESI legacy imaging surveys. They calculated the local density contrast of galaxies within a photometric redshift slice to find the density peaks as cluster candidates. The cluster richness is defined to be the total luminosity of member galaxy candidates and is calibrated using a mass known cluster sample. We find 56 794 CFSFDP clusters detected in this work and the CFSFDP richness is also well correlated with ours by a power law (Fig. 10 d),

$$\log \lambda(\text{CFSFDP}) = (0.70 \pm 0.01) \log \lambda_{500} + (0.48 \pm 0.02). \quad (6)$$

4.1.4 WaZP clusters

Using photometric redshifts of galaxies, Aguena et al. (2021) presented the WaZP algorithm to identify clusters from DES Y1 data covering a sky area of 1511.13 deg^2 . The WaZP algorithm generates a smooth wavelet-based density map within each photometric redshift slice. The overdensity peaks are extracted from the smooth density maps as cluster candidates. The cluster richness is defined to be the sum of the membership probabilities for galaxies brighter than $m^* + 1.5 \text{ mag}$ within a projected distance of r_{200m} . Here, m^* is the characteristic magnitude and r_{200m} corresponds to the radius which the mean density of a cluster is 200 times of the mean density of the universe. The WaZP catalogue contains 60 547 clusters at $0.05 < z < 0.9$, among which 20 131 clusters are detected in this work. However, the WaZP richness has a poor correlation with our richness (Fig. 11). Some clusters with a large value of WaZP richness are poor clusters in our catalogue.

4.2 Comparison with X-ray clusters

Based on the second *ROSAT* All-Sky Survey (RASS) source catalogue (2RXS) and the DES optical data, Klein et al. (2019) identified a sample of X-ray clusters. Optical clusters are found by using a multicomponent matched filter algorithm around the position of the 2RXS sources. A probability of being a random superposition, f_{cont} , is estimated based on the redshift, optical richness

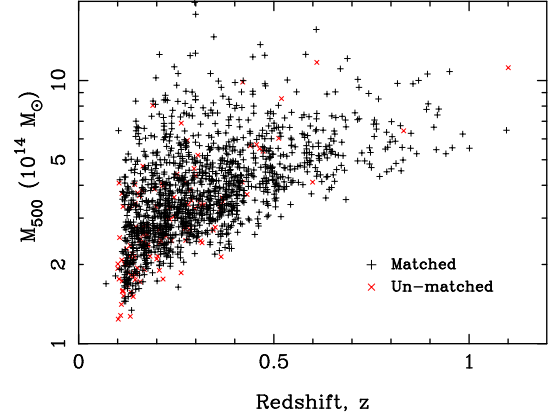


Figure 12. The matched and un-matched RASS X-ray clusters are shown in the redshift-mass diagram.

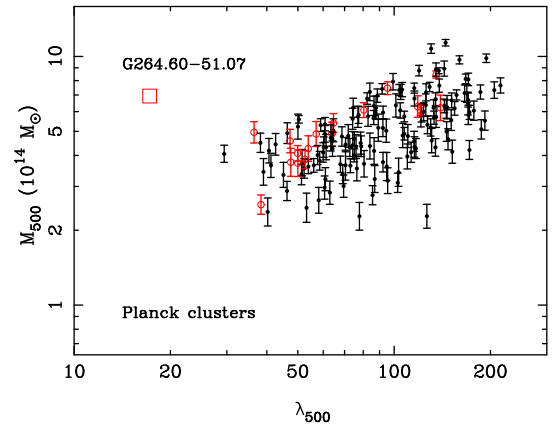


Figure 13. Correlation between cluster mass and our richness for *Planck* clusters. The circles indicate that the clusters have companions with a ratio of their richnesses less than 2. The square indicates an outlier that a more massive foreground cluster is located along the line of sight of this *Planck* cluster.

and implied X-ray luminosity. Their catalogue contains 1953 X-ray clusters at redshifts $0.02 < z < 1.1$ if one sets a probability of $f_{\text{cont}} < 0.1$. Among 1431 X-ray clusters of $z > 0.1$, 1310 (92 per cent) clusters are matched by clusters in our catalogue within a redshift difference of $0.05(1+z)$ and a projected distance of $1.5 r_{500}$. The un-matched X-ray clusters in general have a lower mass (Fig. 12).

Our cluster catalogue can provide redshifts for many X-ray clusters. The XMM Cluster Archive Super Survey (X-CLASS) is a serendipitous search of X-ray clusters from *XMM-Newton* archival observations (Clerc et al. 2012). The X-CLASS catalogue contains 1646 clusters up to $z \sim 1.5$, of which 281 clusters have no redshifts (Koulouridis et al. 2021). Cross-matching the 281 clusters with clusters in our catalogue, we get the redshifts for 45 X-CLASS clusters, as listed in Table A1.

4.3 Comparison with SZ clusters

4.3.1 *Planck* clusters

The *Planck* satellite carries out an all sky millimeter survey with an angular resolution of 5–10 arcmin in the millimeter bands (Planck Collaboration et al. 2020). The second release of the

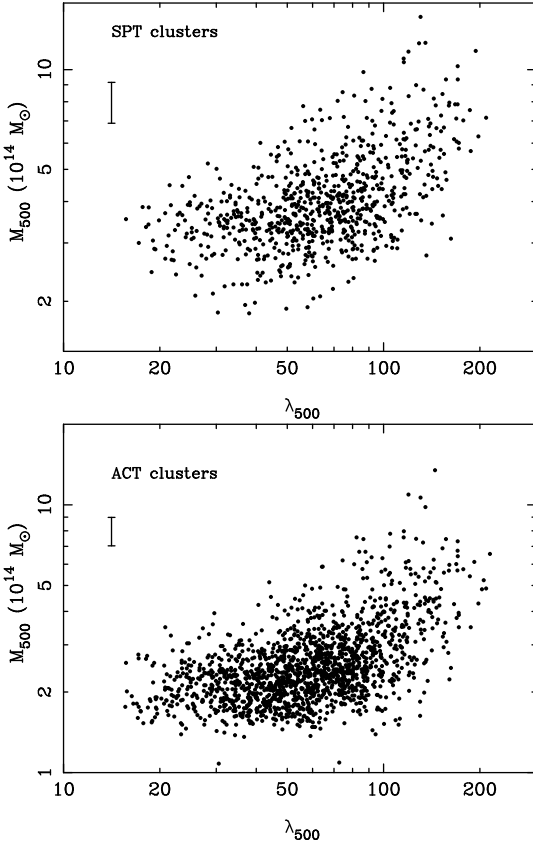


Figure 14. Correlation between cluster mass and our richness for SPT (upper) and ACT (lower) clusters. The error bar indicates the typical uncertainty of the cluster mass in the SZ catalogues.

Planck SZ catalogue contains 1653 clusters, most of which at redshifts $z < 0.5$ (Planck Collaboration et al. 2016). There are 174 *Planck* clusters at $z > 0.1$ in the DES footprint, of which 162 clusters are matched by clusters in our catalogue within a redshift difference of $0.05(1+z)$ and a projected distance of $1.5 r_{500}$. Among the remaining 12 un-matched clusters, 10 clusters are found within a larger redshift difference (see Appendix B). If one also considers the above 10 clusters as matches, our catalogue includes 99 per cent of the *Planck* clusters.

Fig. 13 shows a significant positive correlation between our richness and the *Planck* cluster mass. Within of the *Planck* beam, cluster pairs may be not resolved and both contribute the SZ signal. We find that 23 clusters have a companion cluster within a radius of 5 arcmin and with a ratio of their richness less than 2. With contribution from companion clusters, the matched clusters tend to have a larger mass estimate than other clusters with the same richness. An outlier, PSZ2 G264.60–51.07, has a significant offset from the correlation (red square). Careful checking shows that, along the line of sight towards this cluster, there is a more massive foreground cluster, Abell 3128b at $z = 0.06$ (Piffaretti et al. 2011).

4.3.2 SPT clusters

The SPT observes the southern sky at the frequencies of 95, 150 and, 220 GHz with an angular resolution of 1–1.6 arcmin, making it is an excellent facility to detect SZ clusters (Bleem et al. 2015). Three surveys have been carried out in different regions or with different depths, including SPT-SZ, SPT Extended Cluster Survey

(SPTCS), and SPTpol 100d. The SPT-SZ and SPTCS cluster catalogues contain 677 clusters from a sky area of 2500 deg^2 , 483 clusters from a sky area of 2770 deg^2 , respectively (Bleem et al. 2015, 2020). The SPTpol 100d cluster catalogue contains 89 clusters extending to a lower mass than the SPT-SZ and SPT-ECS (Huang et al. 2020).

In the DES footprint, we get 844 unique SPT clusters at redshifts $0.1 < z \lesssim 1.5$, of which 720 clusters are matched by clusters in our catalogue within a redshift difference of $0.05(1+z)$ and a projected distance of $1.5 r_{500}$. Another 78 SPT clusters can be matched within a redshift difference of $0.05(1+z) - 0.1(1+z)$ from our clusters. Among the remaining 46 un-matched SPT clusters, four of them can be matched within a larger projected distance of $1.5 r_{500} - 2 r_{500}$. Visual inspection shows that these clusters are likely in double cluster systems. Another 18 clusters can be matched within a larger redshift difference. If one considers these clusters as matches, our catalogue includes 97 per cent of the SPT clusters. Fig. 14 (upper panel) shows that our richness has a positive correlation with the SPT cluster mass.

Redshifts of 174 SPT clusters in the DES footprint are unknown and they can be determined by using data in our catalogue. For an SZ cluster located within a projected distance of $1.5 r_{500}$ from an optical cluster, we take the redshift of the optical cluster. Through this procedure, we get redshifts for 56 SPT clusters, as listed in Table A2, of which 15 clusters have redshifts $z > 1$.

4.3.3 ACT clusters

The ACT is designed to detect galaxy clusters at the frequencies of 148 GHz, 218 GHz, and 227 GHz with an angular resolution of 1.4 arcmin at 148 GHz (Swetz et al. 2011). The latest ACT SZ catalogue includes 4195 clusters at redshifts $0.04 < z < 1.95$ from a sky area of $13,211 \text{ deg}^2$ (Hilton et al. 2021), of which 1819 clusters are located in the DES footprint. We find that 1698 (93 per cent) ACT clusters are matched by clusters in our catalogue within a redshift difference of $0.1(1+z)$ and a projected distance of $1.5 r_{500}$. The un-matched matched ACT clusters generally have a low mass. Careful checking the un-matched clusters, we find another eight clusters can be matched by our optical clusters in double cluster systems and 17 clusters can be matched within a redshift difference larger than $0.1(1+z)$. Therefore 95 per cent of ACT clusters can be matched by our clusters. A positive correlation is also found between our richness and the ACT cluster mass (the lower panel of Fig. 14).

4.3.4 Multiple clusters along a line of sight

Multiple clusters can be found along a line of sight due to the projection effect, which may induce bias on cluster mass by SZ and weak lensing effects (White et al. 2002; Shaw et al. 2008; Yuan et al. 2018). Here, we investigate how many SZ massive clusters match multiple optical clusters in the line of sight. An optical cluster is regarded as the counterpart in the line of sight towards an SZ cluster if it is located within a projected distance of r_{500} . We find multiple optical clusters in the line of sight towards 155 SPT clusters and 236 ACT clusters, respectively, as listed in Table A3. Therefore, multiple optical clusters can be found in the line of sight towards about 15 per cent of SZ clusters.

Fig. 15 shows an example that multiple optical clusters located along the line of sight towards an SZ cluster, ACT-CL J0611.3–5937, at $z = 0.39$. Three peaks are clearly shown in the

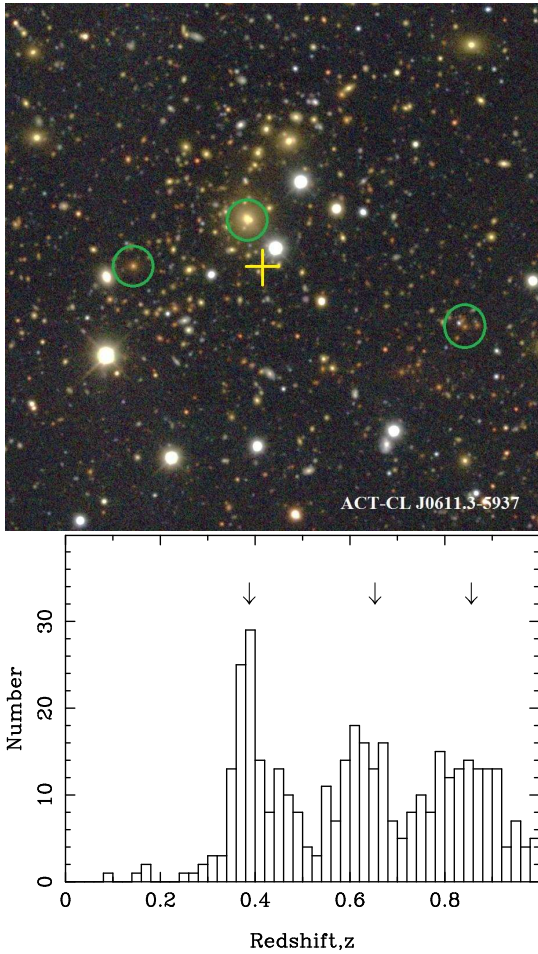


Figure 15. Optical image for an example of multiple clusters along the line of sight towards an SZ cluster, ACT-CL J0611.3–5937, at $z = 0.39$. The image has a size of $4 \text{ arcmin} \times 4 \text{ arcmin}$. In the upper panel, green circles indicate three optical clusters (centring on BCGs) we identify at $z = 0.3643$, 0.6295 and 0.8423 , respectively. The yellow plus indicates the position of the SZ cluster. The lower panel shows the photometric redshift distribution of galaxies within a projected radius 1.5 Mpc from the SZ position. The arrows indicate the redshifts of three optical clusters.

photometric redshift distribution of galaxies, corresponding three clusters at redshifts of 0.3643 , 0.6295 , and 0.8423 with richnesses of 76.00 , 24.88 , and 59.17 , respectively.

5 SUMMARY

We present photometric redshifts for galaxies in the DES \times unWISE data and identify a large sample of galaxy clusters. Using the nearest-neighbour algorithm, we first estimate the photometric redshifts for 105 million DES \times unWISE galaxies. The redshift uncertainty increases from 0.013 at $z \sim 0.1$ to 0.052 at $z \sim 1.3$. The redshift distribution has a peak at $z \sim 0.7$ and extends to $z \sim 1.7$. The stellar mass is derived from the mid-infrared luminosity. Then, we identify a large sample of 151 244 clusters at redshifts $0.1 < z \lesssim 1.5$ based on the overdensity of galaxy stellar mass within a photometric redshift slice. The cluster redshift uncertainty is about 0.013 at redshifts $z < 0.9$. Compared to the published DES cluster catalogues, our catalogue extends to a much higher redshift. We cross-match our clusters with SZ clusters in

the *Planck*, SPT and ACT surveys, and X-ray clusters. More than 95 percent SZ clusters can be matched with clusters in our catalogue. Redshifts are well determined for 45 X-ray clusters and 56 SZ clusters. We find multiple optical clusters in the line of sight towards about 15 percent of SZ clusters.

ACKNOWLEDGEMENTS

We thank the referee for valuable comments that helped to improve the paper. The authors are partially supported by the National Natural Science Foundation of China (Grant Numbers 11988101, 11833009, 12073036 and U1931202), the Key Research Program of the Chinese Academy of Sciences (Grant Number QYZDJ-SSW-SLH021). We also acknowledge the support by the science research grants from the China Manned Space Project with Numbers CMS-CSST-2021-A01, CMS-CSST-2021-A04 and CMS-CSST-2021-B01.

This project used public archival data from the Dark Energy Survey (DES). Funding for the DES Projects has been provided by the U.S. Department of Energy, the U.S. National Science Foundation, the Ministry of Science and Education of Spain, the Science and Technology Facilities Council of the United Kingdom, the Higher Education Funding Council for England, the National Center for Supercomputing Applications at the University of Illinois at Urbana-Champaign, the Kavli Institute of Cosmological Physics at the University of Chicago, the Center for Cosmology and Astro-Particle Physics at the Ohio State University, the Mitchell Institute for Fundamental Physics and Astronomy at Texas A&M University, Financiadora de Estudos e Projetos, Fundação Carlos Chagas Filho de Amparo à Pesquisa do Estado do Rio de Janeiro, Conselho Nacional de Desenvolvimento Científico e Tecnológico and the Ministério da Ciência, Tecnologia e Inovação, the Deutsche Forschungsgemeinschaft, and the Collaborating Institutions in the Dark Energy Survey. The Collaborating Institutions are Argonne National Laboratory, the University of California at Santa Cruz, the University of Cambridge, Centro de Investigaciones Energéticas, Medioambientales y Tecnológicas-Madrid, the University of Chicago, University College London, the DES-Brazil Consortium, the University of Edinburgh, the Eidgenössische Technische Hochschule (ETH) Zürich, Fermi National Accelerator Laboratory, the University of Illinois at Urbana-Champaign, the Institut de Ciències de l’Espai (IEEC/CSIC), the Institut de Física d’Altes Energies, Lawrence Berkeley National Laboratory, the Ludwig-Maximilians Universität München and the associated Excellence Cluster Universe, the University of Michigan, the National Optical Astronomy Observatory, the University of Nottingham, The Ohio State University, the OzDES Membership Consortium, the University of Pennsylvania, the University of Portsmouth, SLAC National Accelerator Laboratory, Stanford University, the University of Sussex, and Texas A&M University. This publication makes use of data products from the Wide-field Infrared Survey Explorer, which is a joint project of the University of California, Los Angeles, and the Jet Propulsion Laboratory/California Institute of Technology, funded by the National Aeronautics and Space Administration. This work makes use of data based on observations made with ESO Telescopes at the La Silla or Paranal Observatories under programme ID(s) 179.A-2004(M) and 179.A-2010(A).

DATA AVAILABILITY

The data of 105 million DES×unWISE galaxies (seven-band magnitudes, photometric redshifts, and stellar masses), 151 244 identified clusters and their 2 454 302 member galaxy candidates are publicly available at http://zmtt.bao.ac.cn/galaxy_clusters/.

REFERENCES

- Abbott T. M. C., et al., 2021, *ApJS*, **255**, 20
 Abell G. O., Corwin Jr. H. G., Olowin R. P., 1989, *ApJS*, **70**, 1
 Agüena M., et al., 2021, *MNRAS*, **502**, 4435
 Ahumada R., et al., 2020, *ApJS*, **249**, 3
 Bleem L. E., et al., 2015, *ApJS*, **216**, 27
 Bleem L. E., et al., 2020, *ApJS*, **247**, 25
 Böhringer H., Chon G., Collins C. A., Guzzo L., Nowak N., Bobrovskiy S., 2013, *A&A*, **555**, A30
 Carlstrom J. E., Holder G. P., Reese E. D., 2002, *ARA&A*, **40**, 643
 Carlstrom J. E., et al., 2011, *PASP*, **123**, 568
 Clerc N., Sadibekova T., Pierre M., Pacaud F., Le Fèvre J. P., Adami C., Altieri B., Valtchanov I., 2012, *MNRAS*, **423**, 3561
 Cool R. J., et al., 2013, *ApJ*, **767**, 118
 Dark Energy Survey Collaboration et al., 2016, *MNRAS*, **460**, 1270
 De Vicente J., Sánchez E., Sevilla-Noarbe I., 2016, *MNRAS*, **459**, 3078
 Hilton M., et al., 2021, *ApJS*, **253**, 3
 Huang N., et al., 2020, *AJ*, **159**, 110
 Klein M., et al., 2019, *MNRAS*, **488**, 739
 Koulouridis E., et al., 2021, *A&A*, **652**, A12
 Lang D., 2014, *AJ*, **147**, 108
 Le Fèvre O., et al., 2013, *A&A*, **559**, A14
 Liske J., et al., 2015, *MNRAS*, **452**, 2087
 Matthews D. J., Newman J. A., Coil A. L., Cooper M. C., Gwyn S. D. J., 2013, *ApJS*, **204**, 21
 Momcheva I. G., et al., 2016, *ApJS*, **225**, 27
 Oguri M., 2014, *MNRAS*, **444**, 147
 Piffaretti R., Arnaud M., Pratt G. W., Pointecouteau E., Melin J.-B., 2011, *A&A*, **534**, A109
 Planck Collaboration et al., 2016, *A&A*, **594**, A27
 Planck Collaboration et al., 2020, *A&A*, **641**, A1
 Rykoff E. S., et al., 2014, *ApJ*, **785**, 104
 Rykoff E. S., et al., 2016, *ApJS*, **224**, 1
 Schlafly E. F., Meisner A. M., Green G. M., 2019, *ApJS*, **240**, 30
 Scodeggio M., et al., 2018, *A&A*, **609**, A84
 Shaw L. D., Holder G. P., Bode P., 2008, *ApJ*, **686**, 206
 Swetz D. S., et al., 2011, *ApJS*, **194**, 41
 Wen Z. L., Han J. L., 2015, *ApJ*, **807**, 178
 Wen Z. L., Han J. L., 2021, *MNRAS*, **500**, 1003
 Wen Z. L., Han J. L., Liu F. S., 2012, *ApJS*, **199**, 34
 Wen Z. L., Han J. L., Yang F., 2018, *MNRAS*, **475**, 343
 White M., Hernquist L., Springel V., 2002, *ApJ*, **579**, 16
 Wright E. L., et al., 2010, *AJ*, **140**, 1868
 Yang X., et al., 2021, *ApJ*, **909**, 143
 Yuan S., Liu X., Pan C., Wang Q., Fan Z., 2018, *ApJ*, **857**, 112
 Zhou Z., et al., 2018, *PASP*, **130**, 085001
 Zou H., et al., 2017, *PASP*, **129**, 064101
 Zou H., et al., 2021, *ApJS*, **253**, 56

APPENDIX A: TABLES OF CROSS-MATCHING WITH X-RAY AND SZ CLUSTER CATALOGUES

In Section 4.2–4.3, we cross-match the clusters in our catalogue with clusters in X-ray and SZ cluster catalogues. We determine redshifts for 45 X-CLASS clusters and 56 SPT clusters, as listed in Tables A1 and A2, respectively. In Table A3, we list multiple optical clusters in the line of sight towards SZ clusters.

APPENDIX B: 12 PLANCK CLUSTERS NOT MATCHED WITHIN A REDSHIFT DIFFERENCE OF $0.05(1+z)$

We find that 10 of 12 un-matched *Planck* clusters have a large uncertainty of redshift and may be matched within a larger redshift difference from our clusters. We present some details if anyone concerns:

PSZ2 G181.71–68.65 has a redshift 0.1529 in the *Planck* catalogue. Along the line of sight, we find a cluster at $z = 0.3176$, which has counterpart cluster with a photometric redshift of $z = 0.3206$ in the CFSFDP catalogue.

PSZ2 G215.19–49.65 has a redshift of 0.2399 in the *Planck*. The redshift is 0.3678 in our catalogue and 0.3607 in the CFSFDP catalogue.

PSZ2 G224.53–30.27 has a redshift of 0.2001 in the *Planck*. Along the line of sight, we identify two clusters, J051657.9–223705 and J051705.8–223654. The cluster, J051657.9–223705, has a redshift of 0.3097 and a richness of 81.26, which has a counterpart cluster at $z = 0.2980$ in the CFSFDP catalogue. The cluster, J051705.8–223654, has a redshift of 0.9844 with a lower richness of 30.46. Thus, PSZ2 G224.53–30.27 is likely matched by the richer cluster at about $z = 0.30$.

PSZ2 G307.72–77.87 has a redshift of 0.4530 in the *Planck*. The redshift is 0.6030 in our catalogue and is 0.5995 in the CFSFDP catalogue.

PSZ2 G261.09–66.14 has a redshift of 0.56 in the *Planck*. The redshift is 0.6418 in our catalogue and is 0.6079 in the CFSFDP catalogue.

PSZ2 G250.59–25.03 has a redshift of 0.55 in the *Planck*. The redshift is 0.6332 in our catalogue and is 0.6249 in the redMaPPer catalogue.

PSZ2 G262.01–32.98 has a redshift of 0.23 in the *Planck*. Along the line of sight, we identify two clusters, J053327.2-542017 and J053304.2-542345. The cluster, J053327.2-542017, has a redshift of 0.2916 and a richness of 33.16, which has a counterpart cluster at $z = 0.3040$ in the redMaPPer catalogue. The cluster, J053304.2-542345, has a redshift of 1.0330 and a larger richness of 33.19. Thus, PSZ2 PSZ2 G262.01–32.98 is contributed from both optical clusters.

PSZ2 G260.76–31.27 has a redshift of 0.25 in the *Planck*. The redshift is 0.3172 in our catalogue and is 0.3141 in the redMaPPer catalogue.

PSZ2 G268.51–28.14 has a redshift of 0.46 in the *Planck*. The redshift is 0.3643 in our catalogue.

PSZ2 G281.09–42.51 has a redshift of 0.38 in the *Planck*. The redshift is 0.5772 in our catalogue and is 0.5550 in the RASS catalogue.

Along the line of sight of two clusters, PSZ2 G212.25–53.20 and PSZ2 G255.64–25.30, no clusters are found in our catalogue with a detection SNR and a richness above the thresholds.

Table A1. 45 X-CLASS clusters with redshifts determined based on our cluster catalogue.

X-CLASS ID (1)	R.A. _X (2)	Dec. _X (3)	MLdet (4)	R.A. (5)	Dec. (6)	z_{cl} (7)	λ_{500} (8)	r_p (9)
551	5.6187	-48.7262	64.52	5.62022	-48.72610	0.9226	33.72	0.028
2716	6.3299	-26.1939	114.75	6.31623	-26.24651	0.4640	68.61	1.140
2226	14.2757	-26.3405	62.70	14.27520	-26.33146	0.4165	44.78	0.179
3138	15.7980	-22.2136	141.56	15.82439	-22.19425	0.2221	26.57	0.402
222	16.0734	-6.7455	75.44	16.07304	-6.74599	0.5827	22.86	0.014
132	19.9576	-44.0768	263.79	19.95924	-44.07513	0.3732	25.67	0.038
98	23.0731	-13.7561	112.05	23.07206	-13.74955	0.5694	42.60	0.156
3271	23.6633	-29.5465	101.07	23.64802	-29.51678	0.4248	25.40	0.653
2958	24.3381	-8.5275	81.63	24.33810	-8.52086	0.7872	35.92	0.178
22690	29.9973	-40.5389	856.32	29.99760	-40.53904	0.7631	37.79	0.007
59	31.9576	2.1567	302.38	31.95749	2.15527	0.8374	19.82	0.039
22724	38.0413	-57.7660	416.02	38.04234	-57.76540	0.5591	39.13	0.019
2831	38.3807	-58.3136	54.14	38.37849	-58.31344	0.6689	36.73	0.030
1998	40.1097	-34.5564	164.90	40.10824	-34.55753	0.2459	24.92	0.023
3357	41.4938	-20.4883	4011.19	41.49205	-20.48772	0.3476	62.24	0.031
2475	52.7173	-38.2198	229.83	52.71795	-38.21850	0.3526	39.19	0.025
2476	52.8683	-38.4078	262.73	52.88900	-38.39761	0.5693	41.33	0.450
2477	52.9013	-38.5544	71.18	52.90094	-38.55338	0.6817	73.57	0.027
380	54.8022	-35.4366	586.46	54.82275	-35.41658	0.5213	24.76	0.586
3246	55.0276	-28.8449	1174.80	55.03021	-28.84417	0.3412	51.92	0.042
3396	55.2673	-18.4472	121.58	55.29052	-18.45590	0.6856	39.80	0.604
24804	55.3873	-54.0582	167.08	55.38786	-54.05875	0.5166	30.51	0.014
24801	55.9383	-53.2460	354.53	55.93827	-53.24508	0.6967	48.00	0.024
3382	56.0465	-54.8537	139.06	56.04767	-54.85653	1.0766	34.74	0.085
2833	56.2025	-54.8733	48.01	56.20447	-54.87134	0.3837	28.47	0.043
22696	58.8494	-59.0921	365.78	58.79378	-59.09582	0.7336	38.78	0.754
21748	61.9848	-21.0035	85.82	61.98438	-21.00267	0.2878	23.65	0.014
3469	63.7497	-58.7290	276.26	63.71315	-58.73209	0.4949	28.27	0.420
461	76.2676	-28.7829	58.70	76.26675	-28.78091	0.5255	22.25	0.048
395	80.8841	-36.6406	108.70	80.88306	-36.64333	1.0064	53.96	0.082
2663	85.8359	-35.9356	474.65	85.83328	-35.93603	0.5929	18.24	0.052
3466	89.3000	-33.0104	201.86	89.27305	-32.96622	0.1443	39.35	0.452
22420	94.0889	-39.6170	579.30	94.08949	-39.61694	0.1560	22.14	0.004
22740	302.7220	-57.3814	799.61	302.72629	-57.38272	0.6469	89.72	0.066
3366	304.6980	-62.9852	161.28	304.69986	-62.98596	0.3655	18.49	0.021
3363	308.1060	-56.3725	65.94	308.05853	-56.43681	0.2955	82.10	1.102
24648	309.6170	-56.2482	81.84	309.60733	-56.25622	0.3723	64.57	0.179
24502	314.7920	-42.8471	121.67	314.79187	-42.84774	0.3465	56.33	0.011
24503	314.9620	-42.8804	88.47	314.96161	-42.87986	1.1197	28.00	0.018
22709	322.6650	-0.2846	34.33	322.66156	-0.28537	0.7476	27.48	0.093
3376	324.0400	-63.1761	250.59	324.03592	-63.17659	0.2299	46.36	0.025
2814	326.5680	-56.7574	109.14	326.59476	-56.77512	0.4954	44.40	0.503
2815	326.6770	-56.8749	237.72	326.67700	-56.87627	0.4901	42.57	0.030
24791	355.1730	-51.4972	73.98	355.17575	-51.50106	0.9692	20.81	0.121
2651	355.3030	-60.9058	158.14	355.33646	-60.90015	0.5047	21.16	0.380

Note. Column 1: ID in X-CLASS catalogue; Column 2 and 3: Right Ascension (R.A. J2000) and Declination (Dec. J2000) of cluster (in degree); Column 4: X-ray detection likelihood; Column 5–6: Right Ascension (R.A. J2000) and Declination (Dec. J2000) of the cluster in our catalogue; Column 7: redshift; Column 8: richness. Column 9: projected separation between the cluster centres in two catalogues, in Mpc.

Table A2. 56 SPT clusters with redshifts determined.

SZ cluster name (1)	R.A. _{SZ} (2)	Dec. _{SZ} (3)	ξ (4)	R.A. (5)	Dec. (6)	z_{cl} (7)	λ_{500} (8)	r_p (9)
SPT-CLJ0013-5714	3.3029	-57.2373	5.11	3.27961	-57.23208	0.6061	27.16	0.330
SPT-CLJ0013-5310	3.4111	-53.1718	4.66	3.40160	-53.17379	0.9003	54.96	0.169
SPT-CLJ0030-4457	7.5150	-44.9640	4.68	7.53638	-44.98155	0.5585	27.02	0.539
SPT-CLJ0034-5554	8.5906	-55.9013	4.54	8.57116	-55.89748	0.9601	39.62	0.329
SPT-CLJ0048-4450	12.1742	-44.8475	4.82	12.17938	-44.84469	0.5950	49.17	0.111
SPT-CLJ0101-3109	15.2898	-31.1514	5.19	15.30829	-31.13954	0.5543	17.85	0.458
SPT-CLJ0105-5358	16.3908	-53.9717	4.53	16.36311	-53.97701	0.7103	20.78	0.443
SPT-CLJ0112-5030	18.0354	-50.5074	4.50	18.00619	-50.50797	0.6775	19.25	0.472
SPT-CLJ0144-4157	26.1463	-41.9601	5.16	26.14669	-41.95748	1.0472	69.93	0.077
SPT-CLJ0146-6126	26.6503	-61.4365	4.87	26.68257	-61.42861	0.8602	46.77	0.479
SPT-CLJ0151-4300	27.8277	-43.0004	4.56	27.82843	-43.00207	1.1521	76.42	0.052
SPT-CLJ0220-2825	35.0214	-28.4171	5.14	35.03450	-28.42431	1.1401	20.47	0.402
SPT-CLJ0220-5445	35.1200	-54.7511	4.57	35.13049	-54.75689	0.7007	34.10	0.216
SPT-CLJ0244-4755	41.0159	-47.9274	4.79	41.00558	-47.89097	0.2604	28.77	0.538
SPT-CLJ0250-4714	42.6656	-47.2385	4.50	42.66674	-47.25129	0.4737	32.74	0.273
SPT-CLJ0256-4221	44.0827	-42.3589	4.54	44.06901	-42.36617	0.8458	16.90	0.343
SPT-CLJ0323-4913	50.9166	-49.2215	4.54	50.89778	-49.19088	0.3881	19.01	0.627
SPT-CLJ0330-2016	52.6254	-20.2713	5.29	52.62220	-20.25523	1.2460	24.27	0.490
SPT-CLJ0337-4442	54.2698	-44.7105	4.84	54.26978	-44.70407	0.9508	59.78	0.183
SPT-CLJ0337-6207	54.4708	-62.1175	5.03	54.47217	-62.10662	0.9633	53.04	0.311
SPT-CLJ0339-3952	54.7862	-39.8734	5.45	54.78075	-39.86796	1.2059	65.61	0.205
SPT-CLJ0353-4818	58.2639	-48.3160	4.90	58.25852	-48.31760	1.0964	32.45	0.115
SPT-CLJ0353-5312	58.3058	-53.2095	4.54	58.32022	-53.19808	0.6205	58.81	0.350
SPT-CLJ0353-5043	58.3853	-50.7278	5.35	58.37934	-50.73331	1.2203	23.84	0.200
SPT-CLJ0430-6251	67.7094	-62.8548	5.29	67.75693	-62.86843	0.5373	27.84	0.584
SPT-CLJ0437-5307	69.2599	-53.1206	4.52	69.26513	-53.09996	0.2885	37.92	0.326
SPT-CLJ0442-4309	70.6940	-43.1528	4.63	70.74709	-43.13006	0.4334	21.00	0.912
SPT-CLJ0447-5041	71.7821	-50.6991	4.62	71.79196	-50.67995	1.3027	19.75	0.607
SPT-CLJ0448-4036	72.0160	-40.6031	4.66	72.02155	-40.60420	1.0942	53.79	0.128
SPT-CLJ0455-2225	73.9549	-22.4246	5.04	73.95729	-22.45580	0.4244	28.21	0.627
SPT-CLJ0500-4713	75.1198	-47.2293	4.92	75.09506	-47.23772	1.2506	35.88	0.563
SPT-CLJ0501-4455	75.2932	-44.9270	4.59	75.26968	-44.93023	0.4557	83.97	0.354
SPT-CLJ0502-6048	75.7229	-60.8112	4.69	75.69482	-60.79540	0.8068	18.28	0.567
SPT-CLJ0534-4847	83.6655	-48.7965	4.59	83.67176	-48.79736	0.7860	58.92	0.113
SPT-CLJ0545-5052	86.4957	-50.8814	4.60	86.49717	-50.87030	0.9295	25.43	0.315
SPT-CLJ0546-6040	86.7342	-60.6723	4.72	86.73521	-60.68235	0.8388	27.16	0.276
SPT-CLJ0548-4340	87.2419	-43.6819	4.59	87.24103	-43.68504	0.8307	24.51	0.088
SPT-CLJ0552-4937	88.1783	-49.6208	5.05	88.18316	-49.60241	0.9929	23.40	0.537
SPT-CLJ0559-6022	89.9419	-60.3832	5.67	89.94439	-60.38390	1.1109	38.83	0.042
SPT-CLJ0601-5204	90.2515	-52.0797	4.54	90.25552	-52.08411	1.0072	24.61	0.146
SPT-CLJ0611-6000	92.7794	-60.0087	4.68	92.80997	-60.01533	0.6466	25.56	0.414
SPT-CLJ2035-5614	308.9018	-56.2402	4.62	308.89615	-56.23104	0.7964	47.34	0.261
SPT-CLJ2106-5820	316.5130	-58.3467	4.65	316.60272	-58.37299	0.2621	36.30	0.786
SPT-CLJ2121-5546	320.2690	-55.7782	4.57	320.27945	-55.78068	1.0916	87.17	0.187
SPT-CLJ2136-5723	324.1203	-57.3968	4.72	324.17242	-57.41769	0.3057	32.52	0.569
SPT-CLJ2139-6430	324.9603	-64.5095	4.53	324.95728	-64.51631	0.9881	58.74	0.199
SPT-CLJ2152-4629	328.1926	-46.4954	4.83	328.18686	-46.49863	0.9300	34.65	0.144
SPT-CLJ2158-4851	329.5692	-48.8533	4.64	329.55301	-48.84221	0.5149	35.83	0.343
SPT-CLJ2233-4729	338.3648	-47.4912	4.59	338.33438	-47.49746	1.1691	26.09	0.638
SPT-CLJ2300-5148	345.0616	-51.8003	4.92	345.03333	-51.78909	0.8232	49.98	0.567
SPT-CLJ2310-5239	347.7022	-52.6609	4.91	347.70789	-52.67169	0.3628	15.49	0.206
SPT-CLJ2328-4616	352.0576	-46.2802	4.84	351.98587	-46.25559	0.2117	28.68	0.688
SPT-CLJ2339-5008	354.9618	-50.1427	4.81	354.95956	-50.14320	0.9275	21.57	0.043
SPT-CLJ2352-5846	358.0510	-58.7758	5.18	358.15778	-58.74107	0.1692	24.63	0.680
SPT-CLJ2357-5953	359.2865	-59.8988	4.67	359.31033	-59.90747	0.5114	22.40	0.328
SPT-CLJ2358-4143	359.6421	-41.7173	4.74	359.61539	-41.73634	1.1105	36.12	0.812

Note. Column 1: Name of SPT cluster; Column 2 and 3: Right Ascension (R.A. J2000) and Declination (Dec. J2000) of SPT cluster (in degree); Column 4: SZ detection significance; Column 5–6: Right Ascension (R.A. J2000) and Declination (Dec. J2000) of the cluster in our catalogue; Column 7: redshift; Column 8: richness. Column 9: projected separation between the cluster centres in two catalogues, in Mpc.

Table A3. Examples for multiple clusters in the line of sight towards 155 SPT clusters and 236 ACT clusters.

SZ cluster name (1)	R.A. _{SZ} (2)	Dec. _{SZ} (3)	SNR (4)	z_{SZ} (5)	R.A. (6)	Dec. (7)	z_c (8)	λ_{500} (9)	θ (10)
SPT-CLJ0010-5112	2.7408	−51.2077	4.51	0.1700	2.74925	−51.20449	0.2077	47.05	0.37
					2.86313	−51.20541	0.7615	18.46	4.60
SPT-CLJ0012-5352	3.0649	−53.8736	4.80	0.3300	3.06954	−53.85092	0.3488	66.51	1.37
					3.08529	−53.85501	0.8924	35.06	1.33
SPT-CLJ0013-4621	3.4715	−46.3563	4.54	0.1800	3.53073	−46.31323	0.1996	37.06	3.56
					3.44134	−46.32892	0.9663	48.29	2.06
.....									
ACT-CLJ0000.7+0225	0.1791	2.4184	6.19	0.4227	0.17833	2.42094	0.4268	29.59	0.16
					0.15072	2.40283	1.0894	18.10	1.94
ACT-CLJ0012.3-5352	3.0875	−53.8750	4.14	0.3431	3.06954	−53.85092	0.3488	66.51	1.58
					3.08529	−53.85501	0.8924	35.06	1.20
ACT-CLJ0014.2-3348	3.5504	−33.8014	6.37	0.4007	3.52542	−33.81221	0.3922	38.11	1.40
					3.55809	−33.80380	0.5370	15.68	0.41

Note. Column 1: Name of SZ cluster; Column 2 and 3: Right Ascension (R.A. J2000) and Declination (Dec. J2000) of SZ cluster (in degree); Column 4: the significance of the SZ detection; Column 5: redshift of SZ cluster; Column 6–7: Right Ascension and Declination of a cluster in our catalogue; Column 8: redshift of the optical cluster; Column 9: cluster richness estimated from the stellar mass. Column 10: angular distance between SZ and optical positions (arcmin).

(This table is available in its entirety in a machine-readable form.)